Outstanding electrochemical performance of highly N- and O-doped carbons derived from pine tannin

Angela Sanchez-Sanchez, Maria Teresa Izquierdo, Sandrine Mathieu, Julia González-Álvarez, Alain Celzard, Vanessa Fierro

Outstanding electrochemical performances of highly N– and O–doped carbons derived from pine tannin

Angela Sanchez-Sanchez[a,*], Maria Teresa Izquierdo[b], Sandrine Mathieu[c], Julia González-Álvarez[d], Alain Celzard[a], Vanessa Fierro[a,*]

Highly N– and O–doped carbons were prepared from pine tannins by hydrothermal carbonisation (HTC) and subsequently applied as materials for supercapacitor electrodes. Pine tannins were transformed into carbon materials by using environment–friendly solvents (water or ammonia) without applying any activation or functionalisation post–treatment. Depending on the solution used for extracting tannins and on the HTC method, carbons with different physicochemical and electrochemical properties were obtained. The material prepared from the water–extracted tannin and submitted to HTC in ammonia displayed a porous texture composed of: a) a low ultramicroporosity and a well–developed mesoporosity; b) a hydrophilic surface with a high density of surface functionalities; and c) a high nanotextural order. These features accounted for the excellent electrochemical performances of the resultant carbon electrodes in terms of high rate capability up to 1 V s^{-1}, high energy density up to ~ 1500 mA g^{-1}, low cell resistance and fast frequency response, making it a suitable material for practical supercapacitors.

1. Introduction

Depletion of fossil fuels and environmental problems caused by pollution makes imperative to change the current model of energy production and consumption. Such a change should inevitably be related to the use of renewable energy sources and the storage and conversion of energy in electrochemical devices, such as batteries and supercapacitors. Supercapacitors are electrochemical energy storage systems that have attracted considerable attention due to their excellent properties, such as high power densities of operation, long life cycle and excellent reversibility.[1,2] Most of the time, they store electric energy through ion accumulation at the electrode/electrolyte interface through an electrochemical double–layer (EDL) mechanism and can be used in a wide range of applications, from portable devices to auxiliary power sources in electric vehicles.

For using them in large–scale industrial applications, many efforts have been devoted to improve their energy densities and to reduce the production costs. Oxygen and/or nitrogen functionalisation of the electrodes has been proved to increase the supercapacitor energy density through pseudocapacitance occurring from Faradaic reactions.[3–5] Numerous types of porous carbons have been tested as material for electrodes, namely activated carbons (AC),[3,6–8] carbon nanotubes,[9–11] graphene,[12,13] carbon aerogels,[14–17] ordered mesoporous carbons,[18–21] etc. Among them, activated carbons obtained from biomass, such as coconut shells,[22] coffee beans,[23] rice husk,[24] algae[25] or tannins[26] have been extensively applied because of their low cost, good chemical stability, easy availability and low toxicity.[27,28] However, biomass-derived ACs most of the time exhibit essentially microporous textures, and those prepared by hydrothermal carbonisation (HTC) followed by activation post-treatments (chemical or physical activation or a combination of both of them) may present a limited surface area.[22]

Tannins are polyphenolic molecules extracted industrially scale from different tree barks (quebracho, mimosa, pine, wattle, etc.) and plants, and mainly applied for the production of adhesives, resins, leather dyes and insulating foams.[29] Tannins have the advantage of being abundant, non-toxic, cheap, and are among the rare reproducible bioressources available at the industrial scale. Obtaining tannins from tree barks normally includes an extraction step, in which bark chips are leached by hot water or an aqueous solution containing salts or additives (sodium hydroxide, sodium sulphite, sodium carbonate or urea), followed by a concentration step.[30–33] Condensed tannins extracted from pine are composed of flavonoid units with numerous reactive hydroxyl groups in positions 3, 5, 7, 3' and 4' (procyanidin), and also possibly in 5' (prodelphinidin) (see **Scheme 1**). They are very interesting

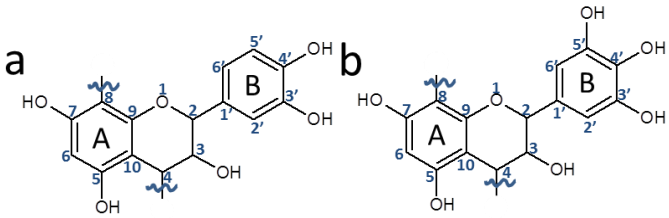

Scheme 1. Chemical structure of the flavonoid unit of a pine condensed tannin: (a) procyanidin; (b) prodelphinidin.

molecules from the chemical point of view, since they can undergo crosslinking reactions through the –OH groups and their reactivity with aldehydes is qualitatively similar to that of phenol and resorcinol, which are much more expensive and toxic molecules.[34]

Using poorly polluting processes for turning biomass into valuable carbon materials is as important as the use of environment–friendly precursors itself. In this sense, hydrothermal carbonisation (HTC) is an easy method that allows obtaining highly oxygen–doped hydrochars under mild

and "green" conditions.[28,35] Hydrochar–derived carbons possess high oxygen contents that might only be achieved by applying oxidation post–treatments when using classical AC synthesis methods instead.[36] However, they exhibit poorly developed porosities that hinder the diffusion of electrolyte ions, especially at high scan rates and current densities at which practical supercapacitors must work.[37] In order to develop their porosities, carbons prepared by HTC are commonly submitted to activation treatments. KOH activation is one of the most used methods since it allows obtaining biomass–derived ACs with surface areas as high as 2000 $m^2 g^{-1}$.[38,39] Nevertheless, it is a time– and energy–consuming method, and the resultant materials must be thoroughly washed to remove the generated by–products, mainly carbonates, thus giving rise to liquid wastes.

In the present work, O– and N–doped porous carbons were prepared through HTC of pine condensed tannins, using water or ammonia as solvents, and subsequent carbonisation. The resultant carbons were not submitted to oxidation or activation post–treatments. The tannin precursors were extracted from barks of *Pinus pinaster* by two processes, either using pure water or an aqueous solution of sodium sulphite and sodium carbonate. Although pine trees are quite abundant in Europe and around the Mediterranean basin, pine tannins have been poorly exploited so far for obtaining high value-added materials**.** The impact of the process used for extracting tannins and of the different HTC procedures on the physicochemical properties of the obtained carbons is investigated here. To the best of our knowledge, this is the first work studying the influence of the extraction process on the physicochemical properties of tannin-derived carbons, and involving favourable economic and environmental outcomes. Finally, the electrochemical behaviour of the carbon materials as supercapacitor electrodes was thoroughly studied and correlated with their physicochemical properties.

2. Experimental

2.1. Materials

Sodium sulphite (95%), sodium carbonate (99.8%) and Folin–Ciocalteu's phenol reagent were purchased from Panreac. Ammonia solution (28 wt.%), sulphuric acid (1M), carbon black powder (< 100 nm) and gallic acid (98%) were purchased from Sigma–Aldrich. Polytetrafluoroethylene (PTFE) and glass fibre separator were provided by Aldrich and Pall Life Sciences, respectively. All the materials were used as received.

2.2. Extraction and concentration of pine tannins

The tannins used in this work were extracted from *Pinus pinaster* by two processes using water or an aqueous solution of sodium salts (2% Na_2SO_3 + 0.5% Na_2CO_3). Both extraction processes were carried out in a Pyrex glass reactor with mechanical stirring and temperature control.

Extraction with water: Pine bark and distilled water, keeping a solid to liquid weight ratio of 1:6, were mixed in the reactor at room temperature. The mixture was heated at 90°C during 90 min, the resultant suspension was filtered under vacuum and the solid residue was washed with distilled water. The obtained extract and the first water leachates were concentrated by spray–drying in a Büchi B-190 Mini Spray Dryer, giving rise to the "W" pine bark tannin.

Extraction with the sodium salt solution: Pine bark and distilled water, in a solid to liquid weight ratio of 1:5, were mixed in the reactor at room temperature and then heated at 75°C. Once this temperature was reached, an aqueous solution containing 2% Na_2SO_3 and 0.5% Na_2CO_3 was added and the resultant mixture was kept at 75°C during 60 min. The suspension was filtered under vacuum and the solid residue was washed with water. Finally, the resultant extract mixed with the first water leachates were concentrated by spray-drying, leading to the "Na" pine bark tannin.

In both cases, the bark residue was dried at room temperature to calculate the extraction yield, i.e., the weight loss percentage of the starting raw material.

2.3. Preparation of the carbon materials

Carbon materials functionalised with oxygen and/or nitrogen were prepared from W and Na pine tannins through hydrothermal carbonisation (HTC) by following the three procedures detailed below:

i) *HTC / water*: tannin (2.0 g) was dissolved in distilled water (16 cm^3) and subsequently submitted to HTC (190°C, 24 h).

ii) *HTC / NH_3*: tannin (2.0 g) was dissolved in a 28 wt.% ammonia solution (16 cm^3) and then submitted to HTC (190°C, 24 h).

iii) *NH_3 evaporation + HTC*: tannin (2.0 g) was dissolved in 28 wt.% ammonia solution (40 cm^3); the mixture was stirred in a sealed flask (20°C, 1 h) and subsequently left for evaporation in a fume hood until complete ammonia evaporation. The resultant powder was dissolved in distilled water (16 cm^3) and submitted to HTC (190°C, 24 h).

The resultant hydrochars were washed with distilled water, dried under vacuum (80°C, 12h) and carbonised in nitrogen atmosphere (900°C, 3h; 1°C min^{-1}).

The final carbons were designated as *Te-x*, where *e* refers to the extraction method (*W*= water or *Na*= sodium salt solution) and *x* to the HTC process: *nothing* for *HTC / water*, *A* for *HTC / NH_3* and *EA* for *NH_3 evaporation + HTC*.

2.4. Characterisation techniques

The total phenol content (TPC) in the extract was determined through the Folin–Ciocalteu method:[40] Folin –Ciocalteu reagent (2.5 mL), previously diluted with water (1:10, v/v), and an aqueous solution of sodium carbonate (2 mL, 75 g L^{-1}) were added to the aqueous solution of extract (0.5 mL); this mixture was heated (50°C, 5 min) and the absorbance was measured (λ = 760 nm) after cooling to room temperature. The phenol content was calculated as the *gallic acid equivalent,* from the calibration curve of gallic acid standard solutions (2–40 µg mL^{-1}), and expressed as the mass of gallic acid equivalent (GAE, g) / 100 g of extract (on dried basis).

The nitrogen adsorption isotherms were obtained at -196°C using a Micromeritics ASAP 2020 automatic system, whereas the carbon dioxide adsorption isotherms were carried out at 0°C with a Micromeritics ASAP 2420. The carbons were degassed at 110°C during at least 48 hours prior to any measurement. This temperature was chosen to avoid heteroatoms evolution at higher temperatures. The surface area was calculated from the nitrogen adsorption isotherms by applying: i) the BET equation, leading to A_{BET}, and ii) the Non-Local Density Functional Theory (NLDFT), leading to S_{NLDFT}. The total pore volume, $V_{0.97}$, was calculated as the amount of nitrogen adsorbed at the relative pressure of 0.97. The micropore volume was calculated by applying the Dubinin–Radushkevich equation to the N_2 and CO_2 isotherms, leading to $V_{\mu\text{-}N2}$ and $V_{\mu\text{-}CO2}$, respectively. The mesopore volume, V_{meso}, was calculated by subtracting $V_{\mu\text{-}N2}$ from $V_{0.97}$. The pore size distributions (PSDs) of the carbons were calculated by applying the NLDFT method for slit pores, provided by the Quantachrome ASWin software, to the nitrogen adsorption isotherms.

Thermogravimetric analysis was carried out in a STA 449F3 Jupiter (NETZSCH) microbalance coupled with a QMS 403D Aëolos (NETZSCH) mass spectrometer working in continuous mode, heating the hydrochar (~ 20 mg) under argon flow up to the target temperature (900°C, 2°C min^{-1}).

Raman spectra were obtained with a Horiba Scientific XploRa Raman spectrometer. The samples were measured as received and the spectra were recorded under a microscope using a 100 × objective. The Raman–scattered light was dispersed by a holographic grating with 1200 lines / mm and detected by a CCD camera. A laser of wavelength 532 nm, filtered at 1% of its nominal power, was used. The incident power (~ 0.1 mW) was low enough to avoid any heating or damage of the samples. Each spectrum was obtained by accumulation of 2 spectra recorded from 800 to 2200 cm^{-1} over 180 s.

Scanning Electron Microscopy (SEM) images were obtained with a FEI-Quanta 400 scanning electron microscope after metallisation.

Elemental analysis was performed with an Elementar Vario EL Cube analyser, measuring CHNS and O separately.

Contact angle between the carbon electrodes and 1M H_2SO_4 electrolyte was measured with a Krüss Drop Shape Analyser using the sessile drop mode and a drop volume of 2 μL.

X–ray photoelectron spectroscopy (XPS) results were recorded with an ESCAPlus OMICROM system equipped with a hemispherical electron energy analyser. The spectrometer was operated at 10 kV and 15 mA, using a non–monochromatised Mg Kα X–ray Source (hν = 1253.6 eV) and under vacuum (< 5 × 10^{-9} Torr). Analyser pass energy of 50 eV was used for survey scans and 20 eV for detailed scans. The C1s peak at 284.5 eV was used for binding energy correction and a survey scan (1 sweep / 200 ms dwell) was acquired between 1100 and 0 eV.

The electrochemical characterisation was performed on a Biologic VMP3 electrochemical workstation. Cyclic voltammetry (CV) and galvanostatic charge–discharge tests (GCD) were carried out in a three–electrode cell, using 1M H_2SO_4 as aqueous electrolyte, a platinum wire as counter electrode and a saturated calomel electrode (SCE) as the reference one. Energy and power densities, as well as cycling stability, were derived from GCD measurements performed in a symmetric two-electrode cell using 1M H_2SO_4 electrolyte. Electrochemical impedance spectroscopy (EIS) measurements were also carried out in a symmetric two–electrode cell with the same electrolyte. The carbon electrodes were prepared by spreading a paste (~ 3 mg) containing the carbon material, polytetrafluoroethylene (PTFE) binder and carbon black in the weight percent ratio of 85:10:5 onto graphite foils. The resultant electrodes were pressed at 5 MPa and impregnated with the electrolyte during 48 hours. The symmetrical supercapacitors were assembled by placing two identical electrodes (active area of 0.503 cm^2) separated by a glass fibre disk between two gold current collectors. CV tests were carried out in the potential window between 0 and 0.9 V at scan rates ranging from 0.5 to 1000 mV s^{-1}. The specific gravimetric capacitance (C, F g^{-1}) was calculated from the CV curves according to **Equation 1**:

$$C = (\int I\,\Delta t) / (s\,\Delta V\,m) \quad (1)$$

where I (A) is the constant current, s (V s^{-1}) is the scan rate, ΔV (V) is the potential window, and m (g) is the mass of active material in the electrode.

GCD tests were carried out in the voltage range between 0 and 0.9 V at charge–discharge current densities ranging from 0.1 to 12 A g^{-1}. Three- or two-electrode cells were used, and the gravimetric capacitances (C and C_{cell}, respectively, expressed in F g^{-1}) were calculated through **Equation 2**:

$$C,\ C_{cell} = (I\,dt) / (m\,dV) \quad (2)$$

where I (A) represents the discharge current, (dV/dt) (V s^{-1}) is the slope of the discharge curve and m is the carbon mass of the single electrode or the two identical electrodes in the three- and two-electrode cells, respectively.

The cycling stability was studied in the same potential range at the current density of 0.5 A g^{-1}, based on the total mass of the two electrodes. From these measurements, gravimetric capacitance (C_{cell}, F g^{-1}), energy density (E, Wh kg^{-1}) and power density (P, W kg^{-1}) were calculated by applying **Equations 2**, **3** and **4**, respectively:

$$E = C_{cell} / 8 \times (\Delta V - IR)^2 \quad (3)$$

$$P = E / \Delta t \quad (4)$$

where ΔV (V) is the potential difference within the discharge time Δt (s), and IR (V) is the voltage drop due to the inner resistance at the beginning of the discharge process.

EIS measurements were performed at open-circuit voltage in the frequency range of 100 kHz – 1 mHz with a 10 mV alternating current amplitude. The gravimetric capacitance (C_{cell}, F g^{-1}) was calculated according to **Equation 5**:

$$C_{cell} = -2\,Im(Z) / (\pi\,f\,|Z|^2)\,m \quad (5)$$

where $-Im(Z)$ (Ω) is the imaginary part of the impedance, f (Hz) is the operating frequency, $|Z|$ (Ω) is the impedance modulus and m (g) is the active material mass for the two electrodes.

3. Results and discussion

3.1. Physico-chemical characterisation

The tests determining the total phenol content evidenced that tannins with different phenolic contents were obtained, depending on the kind of solution used in the extraction process. Tannins extracted with water (W–series tannins) presented 67.9 g GAE / 100 g extract, while tannins extracted with an aqueous solution containing Na_2SO_3/Na_2CO_3 (Na–series tannins) exhibited 89.8 g GAE / 100 g extract. Additionally, extraction yield was also higher for Na–series tannins, 9.8% versus 6.3% for those of the W–series. This finding further supports the use of sulphited solutions instead of pure water for the industrial extraction of tannins.[41]

Nitrogen adsorption isotherms and pore size distributions (PSDs) of the tannin–based carbons are displayed in **Figure 1**. Carbon dioxide isotherms and the corresponding PSDs are shown in **Figure S1** (**Supporting Information** section). The textural parameters, calculated from the nitrogen and carbon dioxide isotherms, are collected in **Table 1**. Clear differences among the adsorption isotherms and the PSDs of the two series of carbon materials were found, as well as among the carbons of each series submitted to different treatments. On the one hand, the isotherm of TW exhibited a very narrow hysteresis loop above a relative pressure of 0.8 (**Figure 1a),** which is associated with large mesopores exhibiting pore diameters wider than 10 nm, as shown in the corresponding PSD (**Figure 1c**). Its porous texture was composed of 38.5% micropores and 61.5% mesopores of sizes ranging from 2 to 30 nm, as calculated from the nitrogen adsorption data collected in **Table 1** and as seen from the PSDs of **Figure 1c**. This carbon exhibited the highest BET area and pore volume of the series, 652 m^2 g^{-1} and 0.65 cm^3 g^{-1}, respectively (**Table 1**). On the other hand, amination treatments gave rise to TW-A and TW-EA materials, whose porous textures were drastically different from each other and from that of TW: i) the plateaus of the TW-A and TW-EA isotherms were shifted to lower values of adsorbed volume, and ii) the hysteresis cycle of TW-EA was broader and appeared at lower relative pressures than for TW and TW-A. This means that the microporosity of both TW-A and TW-EA and the mesopore size distribution of TW-EA changed as a consequence of the amination treatments, and that these changes depended on the type of treatment. Indeed, the micropore volumes decreased by 48% and 20% for TW-A and TW-EA with respect to TW, respectively, while the mesopore volumes remained almost unchanged (**Table 1** and PSDs of **Figure 1c**). Despite having similar mesoporous volumes, TW-EA exhibited a narrower mesopore size distribution than TW and TW-A, as shown in **Figure 1c**. Nevertheless, the samples of the Na–series exhibited totally different porous textures than those of the W–series obtained through the same HTC procedure. The sample prepared by *HTC / water*, TNa, exhibited a poorly developed porous texture (**Figure 1b** and **Table 1**), since A_{BET} and $V_{0.97}$ were as low as 83 m^2 g^{-1} and 0.04 cm^3 g^{-1}, respectively. The sample obtained by *NH_3 evaporation + HTC*, TNa-EA, presented essentially the same poorly developed porous texture as that of TNa, and no significant change could be found between their PSDs (**Figure 1d**). On the contrary, the sample obtained by the *HTC / NH_3* method, TNa-A, exhibited a more developed porous texture than that of TNa. Thus, the values of A_{BET}, $V_{0.97}$ and $V_{\mu\text{-}N2}$ of TNa-A were increased by 81.4, 82.6 and 76.5%, respectively, with respect to the corresponding values of TNa (**Table 1**). The porous texture of TNa-A was composed of 73.9% micropores and 26.1% of mesopores, as calculated from the data obtained from the nitrogen isotherms collected in **Table 1**. The PSD of TNa-A exhibited a relatively narrow distribution of micropores centred at ~ 0.6 nm and a mesopore distribution with pore widths up to 10 nm.

Both carbon series exhibited a fraction of narrow porosity not accessible to nitrogen, as evidenced by two facts: i) the values of the ultramicropore volume calculated from the CO_2 isotherms, $V_{\mu\text{-}CO2}$, were higher than those obtained from the N_2 isotherms, $V_{\mu\text{-}N2}$; ii) the surface areas calculated from the

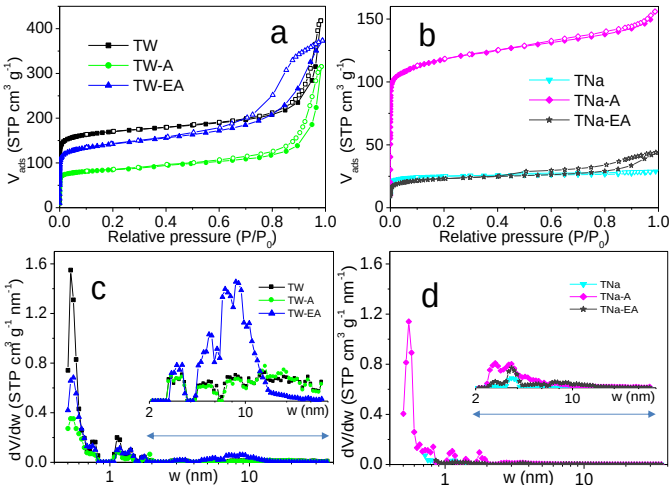

Figure 1. Nitrogen adsorption isotherms measured at -196 °C for the carbons obtained from pine tannins extracted with: (a) water, referred to as W–series, or (b) with sodium salt solution, referred to as Na–series. Pore size distributions (PSDs) of: (c) W–series samples; and (d) Na–series samples.

NLDFT method, S_{NLDFT}, were higher than the BET areas, A_{BET}. Among all the studied carbons, TNa-A exhibited the highest percentage of narrow porosity, 91.3%, as calculated from the values of $V_{\mu\text{-}CO2}$ and $V_{0.97}$ displayed in **Table 1**. The W–series samples presented narrow porosity percentages from 37.9% of TW-EA to 46.2% of TW.

Previous studies proved that the porous texture is progressively developed when pyrolysis temperature increases up to 900°C, mainly due to the release of volatile species. Thus, tannin-derived carbons exhibited surface areas up to 590 m^2 g^{-1} when carbonised at 400°C, and these values increased up to 981 m^2 g^{-1} when carbonised at 900°C.[42] Generally speaking, hydrochars exhibiting higher polymerisation degrees give rise to carbons with lower surfaces areas.[36] Thus, the lower surface areas of TW-A and TW-EA regarding TW can be explained by the higher polymerisation degree of the respective hydrochars due to crosslinking reactions of the N-groups. As shown in **Figure S2** (**Supporting Information** section), aminated hydrochars indeed contain numerous fragments and molecules where N species have substituted –OH groups of raw tannin, to a greater or lesser extent. As evidenced by the CP-MAS ^{13}C NMR and MALDI-ToF results, the hydrochar of TW-A might be a highly polymerised and crosslinked material

where numerous –OH groups were substituted by $–NH_2$ groups, giving rise to a poorly developed porous texture in the resultant carbon. However, hydrochar of TW-EA may exhibit a 3D–gel structure with numerous –NH– bridges, possessing a lower polymerisation degree than the TW-A hydrochar and leading to a more developed porous texture after carbonisation.[36] Gel–type structure of TW-EA was confirmed by SEM (see below). The Na-series materials did not follow the general trend as for the W-series, probably due to the different reactivity of ammonia and/or the presence of salts used for extraction.

The carbonisation yields, being the weight ratio of hydrochars (i.e., samples obtained after HTC treatment) to final carbons (i.e., after subsequent pyrolysis at 900°C), were derived from thermogravimetric analysis (TG) in inert atmosphere. The resulting data and the TG and DTG curves are collected in **Table 1** and **Figure 2a**, respectively. As shown in **Table 1**, carbonisation yields were higher for the samples of the Na–series than for those of the W–series, in agreement with the higher aromatic character of the former. The two samples prepared by *HTC / NH_3*, TW-A and TNa-A, exhibited higher carbonisation yields than those prepared by *NH_3 evaporation + HTC*, TW-EA and TNa-EA. This finding suggests the introduction of higher nitrogen amounts when the first amination method is applied, which will be afterwards confirmed by elemental analysis.

Table 1. Textural parameters calculated from nitrogen and carbon dioxide adsorption isotherms, and carbonisation yield (η) of the carbon materials.

Sample	Nitrogen and carbon dioxide adsorption isotherms						η (%)
	S_{NLDFT} ($m^2 g^{-1}$)	A_{BET} ($m^2 g^{-1}$)	$V_{0.97}$ ($cm^3 g^{-1}$)	$V_{\mu-N2}$ ($cm^3 g^{-1}$)	$V_{\mu-CO2}$ ($cm^3 g^{-1}$)	V_M ($cm^3 g^{-1}$)	
TW	729	652	0.65	0.25	0.30	0.40	51.0
TW-A	336	291	0.49	0.13	0.19	0.36	58.6
TW-EA	520	485	0.58	0.20	0.22	0.38	52.2
TNa	99	83	0.04	0.04	0.16	-	56.2
TNa-A	452	446	0.23	0.17	0.21	0.06	62.4
TNa-EA	68	80	0.07	0.04	0.06	0.03	52.2

Clear differences were observed in the TG and DTG curves of the two series of hydrochars, as shown in **Figure 2a**. In order to identify the possible processes related to the different weight loss steps, the sweep gases were analysed by mass spectrometry. The mass spectrometry profiles for the gases with *m/z* ranging from 18 to 46 released from the TNa-EA hydrochar, as well as the TG/ DTG curves for this sample, are shown in **Figure 2b**. According to previous studies, ammonia reacts during HTC with hydroxyl groups located on the A and B rings of flavonoids and poly-flavonoid tannins, giving rise to N functionalities that induce their oligomerisation and crosslinking.[34] Some of the numerous fragments and oligomers that can be identified in aminated hydrochars by solid state CP-MAS ^{13}C NMR and MALDI-ToF techniques are shown in **Figure S2** (**Supporting Information** section). These molecules contain many hydroxyl, quinone and amino groups, among others, which undergo progressive transformations into more thermally stable species during carbonisation. The emission of gases related to those transformations corresponds to the weight loss stages of the TG curves.

As shown by TG/DTG curves of **Figure 2a**, the decomposition of hydrochars occurred throughout the entire temperature range and no evident plateaus were observed. This means that thermal stability was not reached up to 900°C and it could be indicative of the high functionalisation degree of the hydrochars. The TG curves of the directly aminated hydrochars, TW-A and TNa-A, exhibited a continuous weight loss in the whole range of temperatures, with less pronounced weight loss steps than those of the other samples. These two hydrochars yielded both the lowest weight losses of 41.4 and 37.6 %, respectively, and the lowest evolution of gases, which might indicate the effective stabilisation of poorly stable defects and oxygen groups (carboxylic acids, carbonyls, etc.) by nitrogen doping. Similar stabilisation effects have been observed for graphene oxide (GO) aminated by gaseous NH_3 at temperatures below 200°C.[12] At these low temperatures, NH_3 indeed reacted with the carboxylic groups of GO through a nucleophilic substitution mechanism and generated more thermally stable amide and amine–like functionalities.

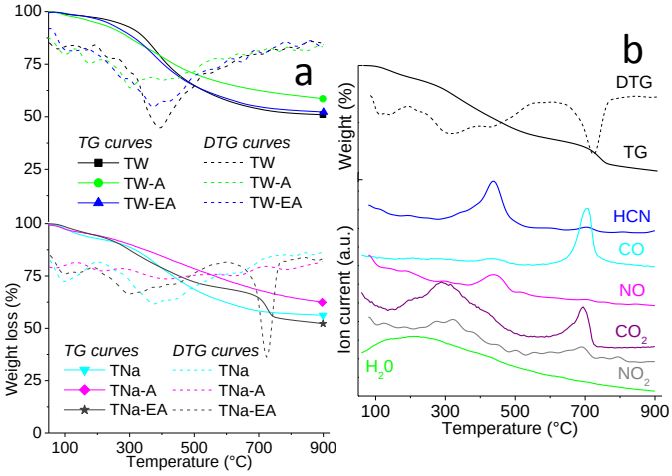

Figure 2. a) TG and DTG curves of all studied hydrochars in argon atmosphere; b) TG (wt.% ranging from 50 to 100%) and DTG curve of the TNa-EA hydrochar (top) and mass spectrometry profiles for output products with *m/z* values ranging from 18 to 46 (bottom).

Regarding the hydrochars prepared by *NH_3 evaporation + HTC*, TW-EA and TNa-EA, both the weight losses (47.8 % in the two cases) and the evolution of gases were slightly higher than for the directly aminated samples, TW-A and TNa-A. This might suggest that the nitrogen doping through *NH_3 evaporation + HTC* exerted a less effective stabilisation effect on the defects and oxygen groups of the hydrochars. The main difference existing between the two amination treatments, *HTC / NH_3* and *NH_3 evaporation + HTC*, is the temperature at which the ammonia reacted with pine tannins: 190°C in the first case and room temperature in the second one. Amination temperature has been proved to exert a key role on the introduction of nitrogen groups in oxygen–doped carbon materials.[12] In light of these TG results, nitrogen doping could be more effective

under hydrothermal conditions. This assumption should be further confirmed from the chemical composition of the final carbons, investigated by elemental analysis and XPS.

As far as processes involved in pyrolysis are concerned, gases released from the studied hydrochars were generally detected up to 500°C (**Figure 2b**). In the case of the aminated hydrochars, such gases were predominantly H_2O, CO_2 and HCN, and CO, NO and NO_2 to a lesser extent. Physisorbed gases, such as water and CO_2, were released from the samples between 25 and ~ 150°C. It is important to note that water evolution was detected up to 700°C, likely due to thermal transformations of certain functional groups (e.g. carboxylic acids) and aromatisation processes giving rise to the final carbons. Below 500°C, CO_2 could evolve from the decomposition of carboxylic acids and carboxylic anhydrides, whereas CO was produced from carboxylic anhydrides and HCN from amine and amide groups. Above 600°C, CO and CO_2 were the gases predominantly released, coming from the decomposition of a wide range of functional groups (phenols, hydroquinones, quinones, carbonyls, lactones and lactols), and low amounts of NO_2 and HCN were also detected.[43–46]

The evolution of NO, NO_2 and HCN was negligible for the non-aminated hydrochars, TW and TNa, in agreement with the low amino acid content of the raw tannins (less than 1 wt.%). In the case of TNa, TNa-A and TNa-EA hydrochars, SO and SO_2 were also released between 160 and 400°C (**Figure S3**), confirming the retention of Na_2SO_3 used in the extraction process. Interestingly, the TG/DTG curves of the TNa-EA hydrochar (**Figure 2b**) evidenced a sharp weight loss centred at 726°C, associated with the release of CO, CO_2, HCN and NO_2. Previous works on nitrogen–doped carbon nanotubes have shown that defective pyridinic–like sites could be repaired by chemisorbed species, adding stability to the carbon nanotubes.[10] These authors observed a slight change in the slope of the TG curve at around 700–720°C for materials doped with high N contents, attributed to possible reactions of the nitrogenated sites (NX, where X = O, N, etc.) located at the surface of the tubes in this range of temperature. Applied to the TNa-EA material, the generated species could be released at higher temperatures and give rise to the pronounced weight loss observed at 726°C.

The bulk chemical composition of the carbon materials was analysed by elemental analysis, and the corresponding results are collected in **Table S1**. 3D Van Krevelen diagrams, showing the relationship between the N/C and S/C atomic ratios versus the O/C and H/C atomic ratios of the materials, are displayed in **Figure 3a** and **3b**, respectively. Given that increasing heteroatom to carbon ratios are related to increasing functionalisation degrees of the materials, Van Krevelen diagrams illustrate the relationship between the material functionalisation and the methods used to extract tannins or to transform them into doped carbon materials. TW and TNa, prepared by *HTC / water*, exhibited the lowest N/C, O/C and H/C atomic ratios, whereas these atomic ratios were the highest for TW-A and TNa-A, synthesised through *HTC / NH_3* (**Figure 3a**). This clearly indicates that *HTC / water* gave rise to the least functionalised samples regarding N and O groups, while *HTC / NH_3* led to the most functionalised ones. Thus, functionalisation of the materials with nitrogen and oxygen groups seemed to be related to the synthesis method, independently of the procedure used for extracting tannins.

With respect to sulphur groups, two samples of the Na–series, TNa and TNa-EA, exhibited the highest S/C ratios, which could be due to the retention of sulphur coming from Na_2SO_3 used in the extraction process (**Figure 3b**). Surprisingly, TW-A and TNa-A presented negligible S/C ratios, so that the *HTC / NH_3* method could induce the removal of sulphur species from the hydrochars. According to this, functionalisation with sulphur groups might depend on both synthesis and extraction methods.

As shown in **Table S1** (**Supporting Information** section), carbons obtained through *HTC / NH_3*, TW-A and TNa-A, possessed the highest nitrogen concentrations, 5.9 and 6.3 wt.%, as well as the highest oxygen contents, 16.4 and 13.2 wt.%, respectively. From the point of view of materials functionalisation, this method was more effective than the *NH_3 evaporation + HTC* method, since it allowed introducing 168 and 163% more nitrogen and 33.3 and 7.3% more oxygen in the TW-A and TNa-A carbons than in the TW-EA and TNa-EA ones, respectively.

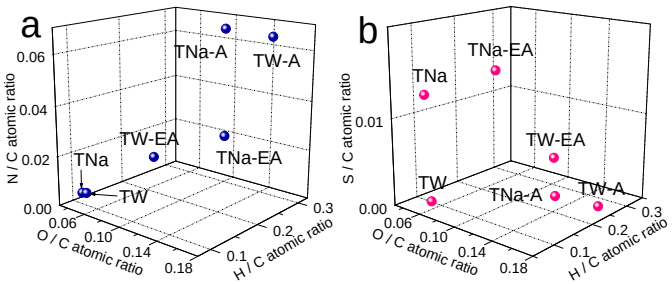

Figure 3. 3D Van Krevelen diagrams showing the relationship between N/C and S/C atomic ratios versus O/C and H/C atomic ratios of the materials (a and b, respectively).

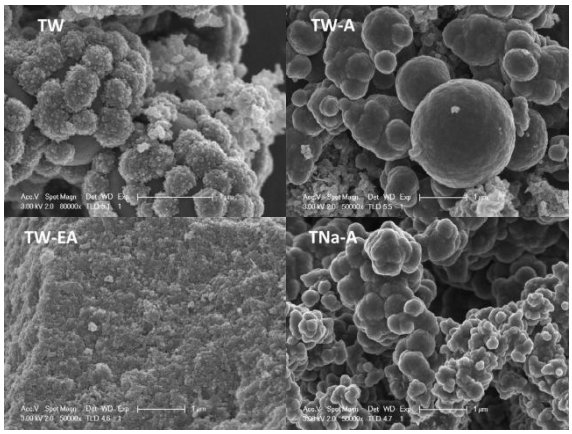

Figure 4. Representative SEM images of the carbon materials.

The morphology of the carbon particles was studied by SEM, and several images of representative materials are shown in **Figure 4**. Tannin-derived hydrochars prepared in hot pressurised water are typically composed of spherical particles whose size depends on the precursor concentration and on the temperature used during HTC.[26,36,47,48] According to these studies, hydrochars obtained at 130–160°C comprise irregular and poly-dispersed spheres; those obtained at 180–190°C exhibit the most spherical particles, whereas those obtained at higher temperatures contain fused particles due to coalescence processes.[49] No remarkable changes in the morphology of the particles were observed after pyrolysis[36,49] and it was thus decided to focus TEM observations only on carbon materials, i.e. after pyrolysis at 900°C.

Carbons synthesised by *HTC / water* method, TW and TNa, were mainly composed of quasi–spherical particles with sizes ranging from 1 to 2 μm, which contained smaller particle aggregates on their surface (400–500 nm diameter). Synthesis methods in the presence of ammonia remarkably changed the particle morphology. On the one hand, the *HTC / NH_3* method, leading to TW-A and TNa-A carbons, reduced the average size of the quasi–spherical particles to 0.1–1 μm and the small surface aggregates were detached from them and dispersed in the carbon bulk. On the other hand, the *NH_3 evaporation + HTC* method gave rise to compact monoliths, TW-EA and TNa-EA, in which no differentiated spherical particles could be distinguished. SEM photographs (**Figure 4**) confirm the 3D-gel structure of TW-EA and TNa-EA samples.

Among the two series of prepared carbons, those presenting more developed porous textures and high bulk nitrogen and oxygen contents were selected in order to study their electrochemical performances. The selected samples were TW, TW-A, TW-EA and TNa-A. Prior to electrochemical characterisation, the nanotexture and the surface chemistry of these materials were investigated by Raman spectroscopy and XPS, respectively.

The first–order Raman spectra collected in **Figure S4** (**Supporting Information** section) presented broad and equally intense D and G bands, characteristic of highly disordered carbon materials.[50] The studied carbons possessed numerous disordered domains and low graphitisation degrees, as indicated by the high width and intensity of the D bands in comparison to those of graphite.[51] The corresponding values of the *I(D) / I(G)* ratios, where *I* is the maximum intensity of each band, known to be related to the graphitisation level,[52] are collected in **Table S2** (**Supporting Information** section). As we deal with non–graphitisable materials, the *I(D) / I(G)* ratios are expected to be proportional to the squared crystallite size, L_a^2.[53] The carbons of the W–series (TW, TW-A and TW-EA) exhibited higher *I(D) / I(G)* ratios than that of the Na–series (TNa-A), so that they possessed larger crystallites and, consequently, slightly less disordered nanotextures than the latter. Among the W–series materials, TW-A exhibited the most ordered nanotexture, since it displayed the highest *I(D) / I(G)* ratio.

One might expect that tannin precursors containing higher contents of phenolic groups lead to more ordered carbons at the nanoscale, since condensation/aromatisation reactions occurring during pyrolysis might be favoured and give rise to larger ordered domains. Keeping in mind that the carbons of the W– and Na–series were prepared from tannins with phenolic group contents of 67.9 and 89.8%, respectively, these results indicate that no direct correlation exist between the initial amount of phenolic groups and the nanotexture of the studied materials.

The data of surface heteroatom concentrations and density of surface nitrogen and oxygen functionalities as obtained by XPS are collected in **Table 2**. No sulphur was found at the carbon surface as determined by XPS. A previous study on HTC–derived carbons demonstrated that the electrochemical behaviour of materials possessing many narrow pores could be better explained in terms of their S_{NLDFT} values instead of A_{BET}, since the latter underestimates the porosity accessible to electrolyte ions.[37] Taking this fact into account, the density of surface functionalities was calculated through the N+O / A_{BET} and N+O / S_{NLDFT} ratios. *HTC / NH_3* was the most effective doping method, since TW-A and TNa-A possessed the highest surface heteroatom concentrations, i.e., 7.96 and 6.37 mmol g^{-1}, respectively. However, the density of surface functionalities, N + 0 / A_{BET}, was 1.91 times higher for TW-A than for TNa-A, and the latter possessed a slightly higher density than that of TW-EA (see **Table 2**). The influence of these density values on the capacitances of the carbon electrodes is discussed below.

Table 2. Surface heteroatom concentrations and density of surface nitrogen and oxygen functionalities of the carbon materials.

Sample	N (mmol g^{-1})	O (mmol g^{-1})	N + O (mmol g^{-1})	N + O / A_{BET} (μmol m^{-2})	N + O / S_{NLDFT} (μmol m^{-2})
TW	0.25	3.61	3.86	5.92	5.29
TW-A	3.25	4.71	7.96	27.35	23.69
TW-EA	0.98	4.97	5.95	12.27	11.44
TNa-A	3.11	3.27	6.37	14.29	14.10

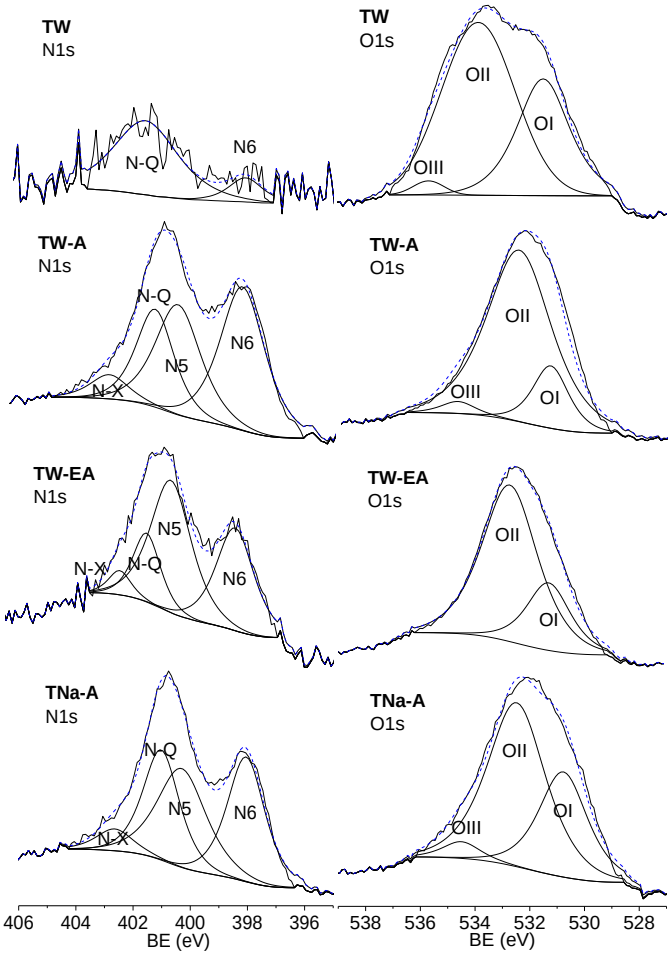

Figure 5. Fitted N1s and O1s high-resolution spectra.

The concentration and type of surface functional groups were determined by fitting the C1s, N1s and O1s high-resolution spectra. **Figure 5** displays the fitted N1s and O1s high–resolution spectra of the materials, and **Table S3** contains the data of binding energy (BE), relative area (A%) and assignments for each contribution. The fit of the N1s peak of TW was not accurate due to its extremely low intensity (**Figure 5**). Preparation methods using NH_3 modified the surface chemistry of the materials not only by introducing nitrogen groups but by slightly changing the relative concentrations of the oxygen groups with respect to the non–doped carbon, TW. It is worth noticing the retention of large relative concentrations of pyridinic and pyrrolic groups after carbonisation of the materials at 900°C, especially if one considers that quaternary nitrogen is usually the predominant group in other nitrogen–doped carbons pyrolysed at the same temperature.[54]

In general terms, TW-A and TW-EA presented higher relative amounts of phenol, ether, ester and anhydride groups than TW, but also lower relative amounts of quinones and carbonyls. Among the nitrogen–doped materials, TW-EA exhibited the highest relative contents of pyrrolic groups and the lowest amounts of quaternary nitrogen. Similar relative concentrations of pyridinic groups were found for TW-EA and TNa-A, 32.2 and 32.9%, respectively, which were slightly higher than that found for TW-A, 27.6%. When comparing the contributions to the O1s peak in TW-A and TNa-A, obtained by *HTC / NH_3*, the latter exhibited higher relative amounts of quinones and carbonyls and lower relative contents of phenols, ethers, ester and anhydride groups (**Table S3**).[55–57]

Figure S5 (**Supporting Information** section) shows the contact angle for the TW-A electrode immediately after a drop of 1M H_2SO_4 was put in contact with the electrode surface. The initial contact angle of the studied electrodes (composed of 85 wt.% carbon + 5 wt.% CB + 10 wt.% PTFE) was lower than 90°, pointing to a hydrophilic character of the surface. No significant differences were found among the contact angle values of the different carbon electrodes, given the high concentrations of N and O functionalities, as determined by XPS, at the surface of the respective carbons. These values were not determined at equilibrium but within a few seconds after the drop deposition, since the electrolyte was progressively absorbed and the contact angle decreased with time. 5 minutes were enough for completely absorbing the drop of 1M H_2SO_4 electrolyte, facilitated by both the porous nature and the hydrophilic character of the studied electrode surfaces.

3.2. Electrochemical characterisation

The electrochemical behaviour of the carbon materials was investigated by cyclic voltammetry and galvanostatic charge–discharge in a three–electrode cell using 1M H_2SO_4 as electrolyte. The resultant cyclic voltammograms (CV) and galvanostatic charge–discharge (GCD) curves within the potential window of 0–0.9 V are shown in **Figure 6**. At the low scan rate of 0.5 mV s^{-1}, all the carbon electrodes exhibited highly distorted CV curves (not shown) with broad redox peaks that indicated the occurrence of Faradaic reactions. As the scan rate increased, the CV curves of the electrodes exhibited quasi–rectangular shape despite their high densities of surface functional groups. This suggests a good capacitive behaviour, since no obvious pseudocapacitive mechanism was evidenced.

It is very important for real devices that the cyclic stability of the cell is not affected when increasing the sweep rates. The CV curves of the W–series electrodes (TW, TW-A and TW-EA) still retained a nearly rectangular shape at the very high scan rate of 1 V s^{-1} (**Figure 6a**), which indicates an excellent rate capability of the materials. However, the slightly spindle–like shape of the CV curves for TW-A and TW-EA, as compared with that of TW, denoted the existence of more kinetic limitations for the electrolyte ions to get into the smaller pores. Contrary to the W–series materials, kinetic limitations were important for TNa-A even at 5 mV s^{-1}, as evidenced by the spindle–like shape and the low anodic and cathodic intensities of the CV curves (**Figure S6**, **Supporting Information**).

On the one hand, high capacitance values of 321 F g^{-1} were achieved by TW at 0.5 mV s^{-1} scan rate, which exhibited the highest surface area and the lowest density of surface functional groups (**Figure 6b**). At this scan rate, TW-A and TW-EA yielded similar capacitance values of 252 and 253 F g^{-1}, respectively, which is quite amazing if we consider that TW-A possessed an A_{BET} 40% lower than that of TW-EA but a density of surface functionalities 55.2% higher than the latter material. On the other hand, the lowest capacitance value of 114 F g^{-1}

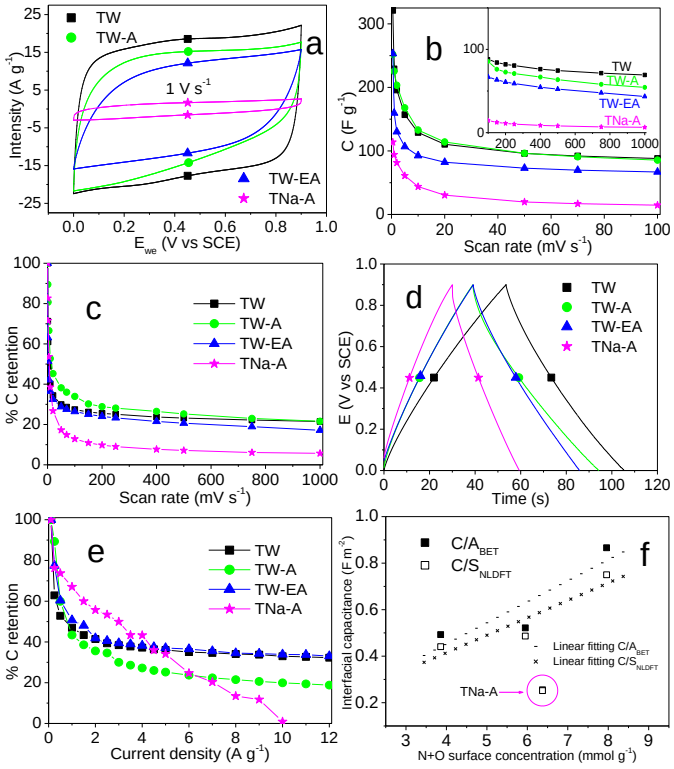

Figure 6. Electrochemical results obtained by CV and GCD with a three – electrode system in 1M H_2SO_4 electrolyte: a) CV curves at 1 V s^{-1}; b) Specific capacitance, calculated from the CV curves, versus the scan rate; c) Percentage of capacitance retention, calculated from the CV curves, versus the scan rate; d) GCD curves measured at 0.5 A g^{-1} current density; e) Percentage of capacitance retention, calculated from GCD curves between 0.1 and 12 A g^{-1} current densities; f) Interfacial capacitances obtained at 0.5 mV s^{-1} versus the heteroatom surface concentration of the carbon materials.

was achieved by TNa-A at 0.5 mV s^{-1} scan rate, despite possessing similar A_{BET} and density of surface functionalities to those of TW-EA. The capacitances of all the materials sharply decreased at scan rates up to 20 mV s^{-1} scan rate and reached a plateau from approximately 100 to 1000 mV s^{-1}, confirming the high rate stability of the materials. The samples of the W–series presented high capacitance retentions at 100 mV s^{-1} of 27.4, 33.9 and 26.4% for TW, TW-A and TW-EA, respectively (**Figure 6c**), while that of the Na–series, TNa-A, exhibited the most pronounced capacitance decrease up to 20 mV s^{-1} and only a capacitance retention of 12.9% at 100 mV s^{-1}.

Bearing in mind that part of the narrow porosity might be unavailable to the electrolyte[7] and considering the different values of capacitance at low scan rate of the materials, the pseudocapacitance contributions of the materials should be investigated. To this end, the interfacial capacitances obtained at 0.5 mV s^{-1} scan rate, C/A_{BET} and C/S_{NLDFT}, were plotted versus the surface heteroatom concentration of the materials (**Figure 6f**). The interfacial capacitances of the electrodes, calculated through C/A_{BET} and C/S_{NLDFT} at 0.5 mV s^{-1}, were proportional to the heteroatom surface concentration, thus evidencing the pseudocapacitive behaviour of the materials. The regression coefficient was slightly higher for C/S_{NLDFT} than for C/A_{BET}, indicating that a portion of the porosity could not be accessible to the electrolyte at this low scan rate. As shown in **Figure 6f**, TNa-A did not follow the same trend as the rest of the materials. Taking into account that this material possessed the highest fraction of narrow porosity, 91.3%, these results could be explained by a highly restricted access of the electrolyte ions to the narrow porosity and also to the surface functionalities; in other words, despite possessing a relatively developed porosity and a high surface heteroatom concentration with respect to the other materials, both characteristics are not totally effective for ion storage at low scan rates, because the electrolyte cannot access the narrow pores.[37] The differences between the interfacial capacitance of TNa-A and the W–series materials progressively decreased as the scan rate increased up to 100 mV s^{-1} (**Figure S7-a**, **Supporting Information**) and to 1 V s^{-1} (**Figure S7-b**, **Supporting Information**), pointing to the existence of more pronounced kinetic limitations for ion transport in the case of the W–series materials. The roughly linear relationship between the interfacial capacitance and the heteroatom concentration was progressively lost as the scan rate increased, as illustrated by the lower values of the correlation coefficients. This is consistent with the occurrence of incomplete redox reactions taking place at the electroactive functional groups under high-sweep rate regimes,[58] thus decreasing the pseudocapacitance contribution to the total capacitance. However, the linear regressions shown in **Figure S7-a** and **S7-b**, evidence a slight pseudocapacitive behaviour of the materials even at the very high scan rate of 1 V s^{-1}, but this affirmation should be supported by studying a larger number of samples.

Galvanostatic charge–discharge (GCD) tests were carried out at current densities from 0.1 to 12 A g^{-1}. At 0.5 A g^{-1} current density, the materials of the W–series presented GCD curves slightly deviated from the triangular shape with no obvious Ohmic drops (**Figure 6d**). This suggests a fast ion transport throughout the material porosity and the occurrence of Faradaic reactions accounting for pseudocapacitance. The specific capacitances, calculated from the discharge curves, were between 258 and 203 F g^{-1} for the W–series materials at the low current density of 0.1 A g^{-1}. TNa-A yielded a much lower capacitance value of 112 F g^{-1} at the same current density and 0.057 V ohmic drop at 0.5 mV s^{-1}, indicative of a hindered ion transport.

The pseudocapacitance contribution of the materials was estimated by GCD in a two–electrode cell and considering the S_{NLDFT} surface area. According to the estimation of Stoeckli and Centeno,[59] TW-A presented the highest pseudocapacitance contribution of 9.7% at 0.1 A g^{-1} current density, which is consistent with its high density of surface functionalities. Functional groups such as quinones, carbonyls, pyridinic and pyrrolic nitrogen are known to participate to Faradaic reactions in sulfuric acid electrolyte, thereby contributing to pseudocapacitance.[60,61] As the current density increased from 0.1 to 2 A g^{-1}, the specific capacitances of TW, TW-A and TW-EA markedly decreased and remained almost constant up to 12 A g^{-1} (**Figure 6e**). TW and TW-EA presented similar capacitance retentions of 32.3 and 33.1%, respectively, at the current density of 12 A g^{-1}, while TW-A reached 21.1%. The differences existing between the capacitance retention of TW-A determined from GCD and that determined from CV suggest

that ion storage is more affected by high current regimes than by high sweep rate regimes. In the case of TNa-A, the capacitance dramatically decreased when higher current densities were applied, making its ability for ion storage vanish at 10 A g^{-1}. The sharp capacitance fading of this material is in agreement with highly restricted access of the electrolyte ions to both the narrow porosity and the surface functional groups.

The energy and power densities and the cycling stability of the supercapacitors made from the studied materials were evaluated through GCD in a two–electrode cell using 1M H_2SO_4 as electrolyte. As shown in the Ragone plot of **Figure 7a**, the W–series carbons exhibited maximal energy densities of 6.7 – 25.22 Wh kg^{-1} under power outputs of 223.6 W kg^{-1} – 19.3 KW kg^{-1}, which clearly exceed those values obtained for other biomass-derived carbons.[37,62,63] TNa-A yielded lower energy and power densities than the rest of the materials in the entire current density interval, in agreement with the results discussed above. Above 3 A g^{-1}, the energy density decreased dramatically and the power density was limited to a maximum value of ~ 4.35 kW kg^{-1}. Cycling stability of the cells was studied at the current density of 0.5 A g^{-1} up to 5000 cycles of charge–discharge (**Figure 7b**). TW exhibited high capacitance retention of 95% up to 2500 cycles of charge–discharge. Above 2500 cycles, the capacitance retention decreased with the number of charge–discharge cycles, probably due to the degradation of electroactive functional groups,[64,65] and reached 77.2% of the initial capacitance after 5000 cycles. The capacitance retention was slightly lower for TW-A than for TW-EA after 5000 cycles, 77.2 and 78.7%, respectively, which can be explained by the partial degradation of the abundant nitrogen and oxygen functionalities, and by their lower surface areas. TNa-A showed a poor cycling stability since the capacitance retention steadily faded as the number of cycles increased, and reached only 40% of the initial capacitance after 5000 cycles.

The Nyquist and frequency response plots obtained from EIS are shown in **Figure 8**, and the data of the corresponding fits to the Nyquist plots are displayed in **Figure S8 (Supporting Information)**. The Nyquist plots were typical of porous electrodes (**Figure 8a**), displaying semicircles at high frequency (10^5 – 10^3 Hz) and straight lines at medium–low frequency (10 – 10^{-3} Hz). TW-EA electrode presented a short 45° Warburg region in the medium frequency range (10^3 – 8 Hz) and the highest equivalent distributed resistance (R_p) of 1.85Ω, com-

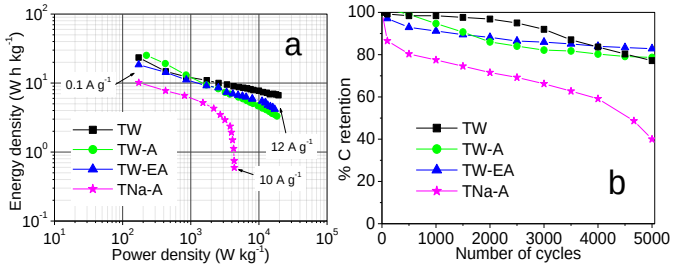

Figure 7. Electrochemical results obtained by GCD with a two–electrode system in 1M H_2SO_4 electrolyte: a) Ragone plot calculated in the current density interval of 0.1 – 12 A g^{-1}; b) Cycling stability, determined from GCD tests at 0.5 A g^{-1} until 5000 cycles.

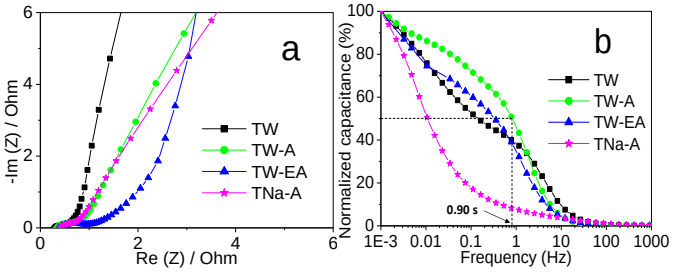

Figure 8. Results obtained by EIS in a two–electrode system with 1M H_2SO_4 electrolyte: a) Nyquist plot; b) Frequency response plot.

monly associated to the resistance for ion transport through the carbon electrodes. The highest equivalent series resistance (*ESR*) found was 2.22Ω, calculated from the intercept with the real impedance axis (*Z'*) of the linear region at low frequency, which indicates that this cell possessed the lowest electrical conductivity. Additionally, TW-EA and TNa-A electrodes exhibited the highest values of electrolyte resistance of 0.37 and 0.38Ω, respectively, calculated as the intercept of the Nyquist plots with the x-axis.

Such higher ion resistances, compared to those determined for the electrodes based on TW and TW-A, are likely due to the high percentages of narrow porosity existing in both carbons together with either low mesoporosity (in TW-EA) or total absence of mesopores (in TNa-A). Interestingly, these values of electrolyte resistance are lower than those obtained for formerly studied biomass–derived carbons and for a wide range of carbon materials.[58,66–69] The low–frequency regions for the TW and TW-EA electrodes were closest to the vertical line than for the TW-A and TNa-A ones, which is associated with high capacitive behaviours and agrees with their lower densities of surface functional groups. The maximal specific capacitance values for the two–electrode system, calculated at 1 mHz, were ~ 50, 34, 31 and 21 F g^{-1} for TW, TW-A, TW-EA and TNa-A, respectively. If these capacitances are calculated for a single electrode, in order to compare them with capacitances obtained from CV and GCD in a three–electrode system, the values are ~ 200, 137, 124 and 85 F g^{-1}, respectively. As expected, the specific capacitances obtained by EIS were lower than those obtained by CV and GCD, since the former were measured in a two–electrode system and the latter in a three–electrode system.

As shown in the frequency response plots (**Figure 8b**), the normalised capacitance decreased when the frequency increased, suggesting that the ion transport was hampered at high–medium frequency (10^3 – 10 Hz). Ion transport was particularly hindered for the TNa-A electrode, since a sharp drop of the normalised capacitance occurred even at very low frequency. This can be explained by the high percentage of narrow porosity and the low mesopore volume of this carbon material, and agrees with the CV and GCD results discussed above. The frequency response time is determined by the relaxation time constant (τ_s), calculated as $1/f_{0.5}$, where $f_{0.5}$ is the frequency at which 50% of the normalised capacitance is achieved. The relaxation time constant for the TNa-A electrode was 65.7 seconds, which means that more than 1 minute is

needed to charge or discharge 50% of the full charge of the supercapacitor. Such high value prevents the use of this material in competitive commercial devices. On the contrary, the TW-A electrode exhibited an extraordinarily fast frequency response of 0.9 s. To the best of our knowledge, this value is one of the lowest ever reported for a broad range of doped and non–doped carbon materials[70–72] and makes the TW-A carbon an excellent candidate as electrode material in real supercapacitors. The frequency response of TW and TW-EA was lower than that of TW-A, since these materials presented relaxation time constants of 7.9 and 3.8 seconds, respectively. Both values were lower than 10 seconds, so TW and TW-EA might also be applied as electrode materials for commercial devices (see **Table S4**, **Supporting Information**).[72]

In summary, the W–series materials yielded better electrochemical performances than the Na–series in terms of high rate capability at high sweep rate regimes, of high capacitance retention at high current density regimes of charge–discharge, of high long–term cycle stability, of higher energy and power densities, even superior to those of a wide range of biomass–derived carbons formerly studied, and of fast frequency responses. Among them, TW-A presented the highest rate capability, the highest energy density up to ~ 1500 mA g^{-1}, one of the lowest cell resistances and the fastest frequency response, making it an appropriate material to be used in real supercapacitors. These excellent performances could be attributed to its low ion diffusion resistance, due to the low percentage of narrow porosity and the high mesopore fraction, the broad PSD in the mesopore range, the hydrophilic character of the electrode surface, the higher nanotexture order, and the high density of nitrogen and oxygen surface functionalities, especially of those involved in Faradaic reactions in acid electrolytes as stated above.

On the contrary, the Na–series material, TNa-A, exhibited a lower rate capability under high sweep rate regimes, and lower cycle stability and energy and power densities than the materials from the W–series. The capability for ion storage was lost at 10 A g^{-1} current density and the frequency response of this carbon material was too slow for using it in a commercial device. Both the restricted ion transport and limited accessibility to the surface functional groups, due to the extremely high narrow porosity percentage, the low mesopore fraction and the less ordered nanotexture might mainly explain the lower electrochemical performances of the TNa-A carbon.

Conclusions

In this work, N– and O–doped carbon materials were successfully prepared by hydrothermal carbonisation of two types of condensed tannins, both extracted from *Pinus pinaster* barks but either with pure water or with an aqueous solution of sodium salts, followed by pyrolysis at 900°C. The electrochemical behaviour of the carbon materials was tested by using an aqueous electrolyte, 1M H_2SO_4, which is less polluting and require less stringent handling conditions than the commonly used organic electrolytes. The green advance is mainly focused on the 4 following points:

1) Condensed pine tannins consist of flavonoid units with numerous hydroxyl groups, whose reactivity with aldehydes is qualitatively similar to that of phenol and resorcinol, which are much more expensive and toxic molecules. Although pine tannins are quite abundant potential resources in Europe and around the Mediterranean basin, they have been poorly exploited so far as biomass precursors for obtaining high value-added materials.
2) The influence of the extraction process of tannins on the physicochemical properties of the resultant carbon materials was studied for the first time: extraction with water led to carbons exhibiting the most appropriate porous textures and the best electrochemical performances.
3) Neither oxidation nor activation post-treatments were applied for further functionalising the materials or for developing their porous texture: this avoids the generation of waste liquids, saves energy and shortens the time for preparing the carbon materials.
4) Chemical functionalisation was performed in one-step through hydrothermal carbonisation (HTC) under mild and environment–friendly conditions and using poorly or non-polluting solvents (water or ammonia), in order to minimise the environmental impact:

    a. HTC in water allowed obtaining highly oxygen-doped hydrochars that produced final carbons exhibiting high oxygen concentrations, normally only achieved by oxidation post-treatments when using classical AC synthesis methods instead.
    b. HTC in ammonia allowed introducing the highest concentrations of N and O surface functionalities, up to 7.96 mmol g^{-1}, on the carbon surfaces. Thus, the carbon obtained from the water–extracted tannin yielded the best electrochemical performances: a high rate capability (up to 1 V s^{-1}), a high energy density up to ~ 1500 mA g^{-1}, a low cell resistance and an extremely fast frequency response, making it a suitable material for practical devices.

Acknowledgements

The IJL research team gratefully acknowledges the financial support of the CPER 2007-2013 “Structuration du Pôle de Compétitivité Fibres Grand’Est” (Competitiveness Fibre Cluster), through local (Conseil Général des Vosges), regional (Région Lorraine), national (DRRT and FNADT) and European (FEDER) funds. Part of this work was supported by CHEERS project (FEDER funds). Dr. Angela Sanchez - Sanchez acknowledges the University of Lorraine, the Region Lorraine and the CNRS for financing her post - Doctoral contract.

References

1 J. R. Miller and P. Simon, *Science*, 2008, **321**, 651–652.
2 P. Simon and Y. Gogotsi, *Nat. Mater.*, 2008, **7**, 845–854.

3 W. Gu, M. Sevilla, A. Magasinski, A. B. Fuertes and G. Yushin, *Energy Environ. Sci.*, 2013, **6**, 2465.
4 J. P. Paraknowitsch and A. Thomas, *Energy Environ. Sci.*, 2013, **6**, 2839.
5 Á. Sánchez-Sánchez, T. A. Centeno, F. Suárez-García, A. Martínez-Alonso and J. M. D. Tascón, *Microporous Mesoporous Mater.*, 2016, **235**, 1–8.
6 W. Feng, P. He, S. Ding, G. Zhang, M. He, F. Dong, J. Wen, L. Du and M. Liu, *RSC Adv*, 2016, **6**, 5949–5956.
7 H. Shi, *Electrochimica Acta*, 1996, **41**, 1633–1639.
8 Y. Ou, C. Peng, J. Lang, D. Zhu and X. Yan, *New Carbon Mater.*, 2014, **29**, 209–215.
9 J. Y. Lee, K. H. An, J. K. Heo and Y. H. Lee, *J. Phys. Chem. B*, 2003, **107**, 8812–8815.
10 F. Villalpando-Paez, A. Zamudio, A. L. Elias, H. Son, E. B. Barros, S. G. Chou, Y. A. Kim, H. Muramatsu, T. Hayashi, J. Kong, H. Terrones, G. Dresselhaus, M. Endo, M. Terrones and M. S. Dresselhaus, *Chem. Phys. Lett.*, 2006, **424**, 345–352.
11 X. Wen, X. Chen, N. Tian, J. Gong, J. Liu, M. H. Rümmeli, P. K. Chu, E. Mijiwska and T. Tang, *Environ. Sci. Technol.*, 2014, **48**, 4048–4055.
12 C.-M. Chen, Q. Zhang, X.-C. Zhao, B. Zhang, Q.-Q. Kong, M.-G. Yang, Q.-H. Yang, M.-Z. Wang, Y.-G. Yang, R. Schlögl and D. S. Su, *J. Mater. Chem.*, 2012, **22**, 14076–14084.
13 Y. J. Oh, J. J. Yoo, Y. I. Kim, J. K. Yoon, H. N. Yoon, J.-H. Kim and S. B. Park, *Electrochimica Acta*, 2014, **116**, 118–128.
14 G. Zu, J. Shen, L. Zou, F. Wang, X. Wang, Y. Zhang and X. Yao, *Carbon*, 2016, **99**, 203–211.
15 Y. Ma, Y. Guo, C. Zhou and C. Wang, *Electrochimica Acta*, 2016, **210**, 897–904.
16 X. Wei, S. Wan and S. Gao, *Nano Energy*, 2016, **28**, 206–215.
17 R. J. White, N. Yoshizawa, M. Antonietti and M.-M. Titirici, *Green Chem.*, 2011, **13**, 2428.
18 C. Vix-Guterl, E. Frackowiak, K. Jurewicz, M. Friebe, J. Parmentier and F. Béguin, *Carbon*, 2005, **43**, 1293–1302.
19 A. B. Fuertes, G. Lota, T. A. Centeno and E. Frackowiak, *Electrochimica Acta*, 2005, **50**, 2799–2805.
20 Y. Xia and R. Mokaya, *Adv. Mater.*, 2004, **16**, 1553–1558.
21 M.-M. Titirici, A. Thomas and M. Antonietti, *J. Mater. Chem.*, 2007, **17**, 3412.
22 A. Jain, V. Aravindan, S. Jayaraman, P. S. Kumar, R. Balasubramanian, S. Ramakrishna, S. Madhavi and M. P. Srinivasan, *Sci. Rep.*, 2013, **3**.
23 T. E. Rufford, D. Hulicova-Jurcakova, Z. Zhu and G. Q. Lu, *Electrochem. Commun.*, 2008, **10**, 1594–1597.
24 X. He, P. Ling, M. Yu, X. Wang, X. Zhang and M. Zheng, *Electrochimica Acta*, 2013, **105**, 635–641.
25 M. Sevilla, W. Gu, C. Falco, M. M. Titirici, A. B. Fuertes and G. Yushin, *J. Power Sources*, 2014, **267**, 26–32.
26 F. L. Braghiroli, V. Fierro, A. Szczurek, N. Stein, J. Parmentier and A. Celzard, *Ind. Crops Prod.*, 2015, **70**, 332–340.
27 Z. Zhub, *Green Carbon Mater. Adv. Appl.*, 2014, 93.
28 J. A. Libra, K. S. Ro, C. Kammann, A. Funke, N. D. Berge, Y. Neubauer, M.-M. Titirici, C. Fühner, O. Bens, J. Kern and K.-H. Emmerich, *Biofuels*, 2011, **2**, 71–106.
29 P. Schofield, D. . Mbugua and A. . Pell, *Tann. Biol. Eff. Rumin. Feeds*, 2001, **91**, 21–40.
30 I. E. H. Elgailani and C. Y. Ishak, *Pak. J. Anal. Environ. Chem.*, 2016, **17**.
31 R. Naima, M. Oumam, H. Hannache, A. Sesbou, B. Charrier, A. Pizzi and F. Charrier – El Bouhtoury, *Ind. Crops Prod.*, 2015, **70**, 245–252.
32 S. Bianchi, I. Kroslakova, R. Janzon, I. Mayer, B. Saake and F. Pichelin, *Phytochemistry*, 2015, **120**, 53–61.
33 G. Vázquez, J. González-Alvarez, S. Freire, F. López-Suevos and G. Antorrena, *Holz Als Roh- Werkst.*, 2001, **59**, 451–456.
34 F. Braghiroli, V. Fierro, A. Pizzi, K. Rode, W. Radke, L. Delmotte, J. Parmentier and A. Celzard, *Ind. Crops Prod.*, 2013, **44**, 330–335.
35 S.-M. Alatalo and others, *Acta Univ. Lappeenrantaensis*, 2016.
36 F. L. Braghiroli, V. Fierro, M. T. Izquierdo, J. Parmentier, A. Pizzi, L. Delmotte, P. Fioux and A. Celzard, *Ind. Crops Prod.*, 2015, **66**, 282–290.
37 A. Sanchez-Sanchez, A. Martinez de Yuso, F. L. Braghiroli, M. T. Izquierdo, E. D. Alvarez, E. Pérez-Cappe, Y. Mosqueda, V. Fierro and A. Celzard, *RSC Adv*, 2016, **6**, 88826–88836.
38 K. Kierzek, E. Frackowiak, G. Lota, G. Gryglewicz and J. Machnikowski, *Electrochimica Acta*, 2004, **49**, 515–523.
39 M. S. Balathanigaimani, W.-G. Shim, M.-J. Lee, C. Kim, J.-W. Lee and H. Moon, *Electrochem. Commun.*, 2008, **10**, 868–871.
40 V. L. Singleton and J. A. Rossi, *Am. J. Enol. Vitic.*, 1965, **16**, 144.
41 A. Pizzi, in *Monomers, Polymers and Composites from Renewable Resources*, Mohamed Belgacem, Alessandro Gandini, 1st Edition., 2008, p. 188.
42 F. L. Braghiroli, V. Fierro, J. Parmentier, A. Pasc and A. Celzard, *Green Chem*, 2016, **18**, 3265–3271.
43 R. Arrigo, M. Hävecker, R. Schlögl and D. S. Su, *Chem. Commun.*, 2008, 4891.
44 J. L. Figueiredo, *J. Mater. Chem. A*, 2013, **1**, 9351.
45 J. L. Figueiredo, M. F. R. Pereira, M. M. A. Freitas and J. J. M. Orfao, *carbon*, 1999, **37**, 1379–1389.
46 M. S. Shafeeyan, W. M. A. W. Daud, A. Houshmand and A. Shamiri, *J. Anal. Appl. Pyrolysis*, 2010, **89**, 143–151.
47 M. Li, W. Li and S. Liu, *Carbohydr. Res.*, 2011, **346**, 999–1004.
48 *Sustainable carbon materials from hydrothermal processes*, Maria-Magdalena Titirici, 1st edition., 2013.
49 F. L. Braghiroli, V. Fierro, M. T. Izquierdo, J. Parmentier, A. Pizzi and A. Celzard, *Bioresour. Technol.*, 2014, **151**, 271–277.
50 V. Barranco, M. A. Lillo-Rodenas, A. Linares-Solano, A. Oya, F. Pico, J. Ibañez, F. Agullo-Rueda, J. M. Amarilla and J. M. Rojo, *J. Phys. Chem. C*, 2010, **114**, 10302–10307.
51 V. N. Tsaneva, W. Kwapinski, X. Teng and B. A. Glowacki, *Carbon*, 2014, **80**, 617–628.
52 D. L. Perry and A. Grint, *Fuel*, 1983, **62**, 1024–1033.
53 A. C. Ferrari and J. Robertson, *Phys. Rev. B*, 2000, **61**, 14095.
54 F. Su, C. K. Poh, J. S. Chen, G. Xu, D. Wang, Q. Li, J. Lin and X. W. Lou, *Energy Env. Sci*, 2011, **4**, 717–724.
55 D. Briggs, *Surface Analysis of Polymers by XPS and Static SIMS*, Cambridge University Press, 1998.
56 A. B. Dongil, B. Bachiller-Baeza, A. Guerrero-Ruiz, I. Rodríguez-Ramos, A. Martínez-Alonso and J. M. D. Tascón, *J. Colloid Interface Sci.*, 2011, **355**, 179–189.
57 C. Weidenthaler, A.-H. Lu, W. Schmidt and F. Schüth, *Microporous Mesoporous Mater.*, 2006, **88**, 238–243.
58 D. Wang, Z. Geng, B. Li and C. Zhang, *Electrochimica Acta*, 2015, **173**, 377–384.
59 T. A. Centeno and F. Stoeckli, *Electrochimica Acta*, 2011, **56**, 7334–7339.
60 M. Inagaki, H. Konno and O. Tanaike, *J. Power Sources*, 2010, **195**, 7880–7903.
61 E. Frackowiak and F. Beguin, *Carbon*, 2001, **39**, 937–950.
62 H. Chen, D. Liu, Z. Shen, B. Bao, S. Zhao and L. Wu, *Electrochimica Acta*, 2015, **180**, 241–251.
63 A. Jain, C. Xu, S. Jayaraman, R. Balasubramanian, J. Y. Lee and M. P. Srinivasan, *Microporous Mesoporous Mater.*, 2015, **218**, 55–61.
64 C.-T. Hsieh and H. Teng, *Carbon*, 2002, **40**, 667–674.
65 A. G. Pandolfo and A. F. Hollenkamp, *J. Power Sources*, 2006, **157**, 11–27.
66 M. Zhou, F. Pu, Z. Wang and S. Guan, *Carbon*, 2014, **68**, 185–194.

67 H. Zhang, L. Zhang, J. Chen, H. Su, F. Liu and W. Yang, *J. Power Sources*, 2016, **315**, 120–126.
68 C. Long, J. Zhuang, Y. Xiao, M. Zheng, H. Hu, H. Dong, B. Lei, H. Zhang and Y. Liu, *J. Power Sources*, 2016, **310**, 145–153.
69 Y.-Q. Zhao, M. Lu, P.-Y. Tao, Y.-J. Zhang, X.-T. Gong, Z. Yang, G.-Q. Zhang and H.-L. Li, *J. Power Sources*, 2016, **307**, 391–400.
70 W. Xing, S. Z. Qiao, R. G. Ding, F. Li, G. Q. Lu, Z. F. Yan and H. M. Cheng, *Carbon*, 2006, **44**, 216–224.
71 H. Wang, Z. Li, J. K. Tak, C. M. B. Holt, X. Tan, Z. Xu, B. S. Amirkhiz, D. Harfield, A. Anyia, T. Stephenson and D. Mitlin, *Carbon*, 2013, **57**, 317–328.
72 L. Wei, M. Sevilla, A. B. Fuertes, R. Mokaya and G. Yushin, *Adv. Energy Mater.*, 2011, **1**, 356–361.